Comprehensive Characterization of an Ellipsoidal Cylinder Calibrator for Radar Cross Section Measurement

Tianjin Liu, Xiaoyu He, and Xiaojian Xu

***Abstract*— Currently, a set of scaled squat circular cylinders (SCCs) have been widely used for co-polarimetric radar cross section (RCS) calibration in various test ranges where low RCS metal pylons are used. The major drawback of a circular cylinder (CC) is its high sensitivity to elevation angle, as well as the frequency-dispersive theoretical RCS. In this work, we propose a new RCS calibrator, the metal ellipsoidal cylinder (EC), whose RCS characteristics are similar to a metal sphere, while it can be mounted on a metal pylon with little electromagnetic (EM) interactions as a CC does. A high-frequency RCS expression is derived using geometrical optics (GO) for the new calibrator. The scattering mechanisms are analyzed to establish the accurate parametric representation of the theoretical RCS. Based on surface current analysis and numerical calculation, the calibrator-pylon interaction (CPI), the angular sensitivity, and the bistatic RCS characteristics are discussed, enabling the calibration uncertainty evaluation for applying the proposed calibrator in the ground-plane range (GPR). Numerical and experimental results of a manufactured squat EC (SEC) are presented to demonstrate the excellent performance of the proposed EC calibrator for co-polarimetric RCS calibration.**

***Index Terms*— Electromagnetic (EM) scattering, ground-plane range (GPR), radar cross section (RCS) measurement, RCS calibrator, surface current.**

I. Introduction

IN RADAR cross section (RCS) measurement using a relative calibration technique, the exact relation between the received echo and the RCS of the target under test is established by a standard calibrator [1]–[3]. From practical applications [4], the characteristics of a well-behaved calibrator include: 1) the theoretical RCS of the calibrator can be accurately calculated over all measurement frequencies and the applicable angles; 2) its RCS should be insensitive to a certain range of angles; 3) the interaction between the calibrator and the pylon is small enough such that its impact on RCS measurement uncertainty may be negligible; and 4) the calibrator is easy to manufacture.

Traditional calibrators such as spheres, circular cylinders (CCs), flat plates, and corner reflectors have been well used for different RCS calibration processes [3], [5]. A metal sphere is an isotropic conductor whose RCS is insensitive to the angle of incident electromagnetic (EM) wave and radar frequency, while the theoretical RCS can be precisely calculated using the Mie series [6]. However, when mounted on a low RCS pylon as almost every advanced RCS test range is equipped with, the interactions caused between the sphere and the pylon are unacceptable [4]. For the use of low RCS pylon as target support, a set of scaled squat CCs (SCCs) with a diameter-to-height ratio (DHR) of 15:7 have been widely adopted for both indoor and outdoor RCS ranges [7]–[10]. In previously published works, Xu *et al.* [9] have analyzed the mechanisms of such a set of SCCs and proposed a fast and accurate calculation of the theoretical RCS, which is based on the complex exponential (CE) model representation of the numerical data from the method of moment (MoM). Although the SCC can be well applied to the pylon with low interaction, its RCS is sensitive to elevation angle, especially in higher frequency bands [10], limiting its application in some RCS test fields, such as an outdoor ground-plane range (GPR) and RCS ranges where multiple-input and multiple-output (MIMO) or phased antenna arrays are used [10], [11].

In order to overcome the RCS sensitivity to the elevation angle of SCCs, Kent *et al.* [12] proposed a specially shaped hypergeoid calibrator whose RCS is insensitive to the elevation angle with limited success. Li *et al.* [13] proposed a spheroidal cylinder calibrator changing the side face from cylindroid to spheroid, whose major drawback is that the RCS level becomes a little bit too low for a high signal to clutter ratio (SCR) requirement. Liang and Xu [14] proposed an ellipsoidal CAM (ECAM) calibrator that changed the side of a CAM proposed by Wood *et al.* [15] and Naiva *et al.* [16] to an ellipsoidal surface for multiple calibration uses. Due to the complexity of its geometry, the characteristics of the ECAM calibrator have not yet been analyzed comprehensively.

In this article, starting from the ECAM work, we focus on developing a new calibrator, named ellipsoidal cylinder (EC), for RCS measurement. Different from the fully-polarimetric RCS calibration devices [17], [18], the new calibrator is made for co-polarimetric RCS calibration. In the high-frequency region, the RCS characteristics of the proposed calibrator are similar to a metal sphere which is insensitive to the radar frequency and elevation angle. Meanwhile, it can be adopted to a low RCS pylon with little EM interactions as a CC does.

The remainder of the context is organized as follows. The three-dimensional (3-D) geometry, scattering mechanisms,

Manuscript received 25 November 2021; revised 12 March 2022; accepted 1 April 2022. Date of publication 25 April 2022; date of current version 6 October 2022. *(Corresponding author: Xiaojian Xu.)*

The authors are with the School of Electronics and Information Engineering, Beihang University, Beijing 100191, China (e-mail: tianjinliu@buaa.edu.cn; hexiaoyu@buaa.edu.cn; xiaojianxu@buaa.edu.cn).

Color versions of one or more figures in this article are available at https://doi.org/10.1109/TAP.2022.3168737.

Digital Object Identifier 10.1109/TAP.2022.3168737

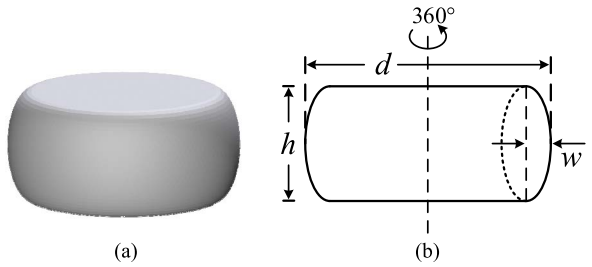

Fig. 1. Geometry of the EC calibrator. (a) Isometric view. (b) Cross section of the front view.

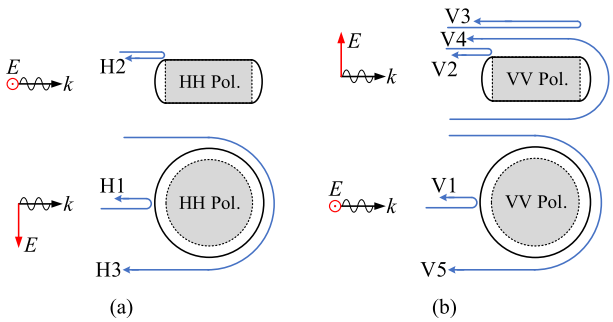

Fig. 2. Scattering mechanisms of an SEC calibrator. (a) HH polarization. (b) VV polarization.

and parametric representation of the proposed EC calibrator are discussed in Section II. The calibrator-pylon interaction (CPI) for CC and EC calibrators is analyzed in Section III. In Section IV, the monostatic and bistatic angle variant RCS characteristics are studied using MoM and geometrical optics (GO) approximation. The calibration uncertainty in GPR is discussed in terms of elevation angle sensitivity in Section V. The measurement results are presented in Section VI with analysis to validate the proposed EC calibrator. We summarize the article in Section VII.

II. Geometry, Scattering Mechanism, and Parametric Representation

A. Geometry and GO Solution of the Theoretical RCS

With the ellipsoidal surface added to the side of an upright cylinder, the 3-D geometry of the proposed EC is shown in Fig. 1, which is determined by three parameters, i.e., the diameter of the calibrator d, the height or the long axis of the ellipsoid h, and the width or the short axis of the ellipsoid w.

According to the GO expression of hyperboloids at higher frequency bands [19], [20], when the elevation angle θ, defined as the radar line of sight (LOS) bias from broadside incidence, is small, the analytical expression of the RCS for the EC can be derived using differential geometry [21]. A detailed derivation can be found in Appendix-A. The RCS formula given as (52) in the Appendix is duplicated here for convenience

$$\sigma_{\mathrm{GO}}(\theta) = \frac{\pi h^2 w^2 \left[(d-2w)\sqrt{(h\sin\theta)^2+(2w\cos\theta)^2}+4w^2\cos\theta\right]}{\cos\theta\left[(h\sin\theta)^2+(2w\cos\theta)^2\right]^2} \tag{1}$$

for $w > \lambda/8$ with λ being the radar wavelength.

For normal broadside incidence of EM wave ($\theta = 0$), the GO formula of RCS is

$$\sigma_{\mathrm{GO}}(0) = \frac{\pi d h^2}{8w}, \quad w > \lambda/8. \tag{2}$$

When w is equal to $h/2$, the EC becomes a spheroidal cylinder as discussed in [13]. Therefore, it can be seen that the spheroidal cylinder calibrator is in fact a special case of the EC calibrator.

B. Backscattering Mechanism Analysis

In practical engineering applications, the diameter-to-height-to-width ratio (DHWR) of the EC calibrator can be changed for different RCS levels and angular sensitivities to satisfy the requirements for different RCS measurements. In order to compare with the characteristics of a standard SCC calibrator whose DHR is 15:7, a squat EC (SEC) calibrator is analyzed, whose DHWR is 15:7:1.5. The SEC's ratio parameter is a compromised design between RCS level and sensitivity to elevation angle. The SEC's RCS is close to that of a sphere with the same diameter, shown in Appendix C. In the following discussions, the SEC is taken as an example.

The backscattered field of an SEC calibrator consists of three different mechanisms, i.e., the GO scattering (specular reflection wave), the surface waves (traveling and creeping waves), and the second-order diffraction wave component. The scattering mechanisms of horizontally (HH) and vertically (VV) polarizations are illustrated in Fig. 2(a) and (b), respectively, where the arrow of E represents the direction of electric field polarization, and k is the incident direction of EM wave. The number markers represent different scattering centers (SCs) which are detailed in Table I, where the location of the SCs refers to the geometric center of the calibrator. Table II lists the correlation between the SCs and the geometrical parameters for VV polarization, where "P," "N," and "U" represent positively correlated, negatively correlated, and uncorrelated, respectively.

The backscattering ultrawideband (UWB) RCS amplitude and phase data of a 15 in diameter SEC calibrator from 10 MHz to 12 GHz with a 10 MHz frequency step are calculated using the MoM code of FEKO software [22], as shown in Fig. 3. The solid, dash-dotted, and the dashed lines in Fig. 3 denote, respectively, the MoM results for HH, VV polarization and the backscattering GO solution. A time-frequency analysis of the UWB RCS data clearly demonstrates the scattering mechanisms, as shown in Fig. 4, where Fig. 4(a) and (b) demonstrate the time–frequency representations (TFRs) of the one-dimensional (1-D) high-resolution range profiles (HRRPs) varying with radar frequency for HH and VV polarizations, respectively. The marked SCs in Fig. 4 are, respectively, corresponding to the indices as seen in Fig. 2(a) and (b).

It is seen from the TFRs in Fig. 4 that the specular reflection components H1 and V1 are independent of the frequency,

TABLE I
SCATTERING MECHANISMS OF THE SEC CALIBRATOR

Polarization	SC	Location	Mechanism
HH	H1	$r_1 = -d/2$	Specular reflection of the front ellipsoid.
	H2	$r_2 = -d/2 + w$	Diffraction wave from second-order differential discontinuity.
	H3	$r_2 = \pi d/4$	Creeping wave that moves along the side of ellipsoid through the shadowed region.
VV	V1	$r_1 = -d/2$	Specular reflection of the front ellipsoid.
	V2	$r_2 = -d/2 + w$	Diffraction wave from second-order differential discontinuity.
	V3	$r_3 = d/2 - w$	Travelling wave reflected by the rear differential discontinuity.
	V4	$r_4 = [d + h + (\pi - 4)w]/2$	Surface wave that first travels along the upper and lower surfaces, then creeps along the shadowed region , and finally return along the lower and upper surfaces.
	V5	$r_5 = \pi d/4$	Creeping wave that moves along the side of ellipsoid through the shadowed region.

TABLE II
CORRELATION BETWEEN SCS AND GEOMETRICAL PARAMETERS

Parameter \ SC	V1	V2	V3	V4	V5
d	P	U	P	P	N
h	P	P	U	N	U
w	N	N	N	N	U

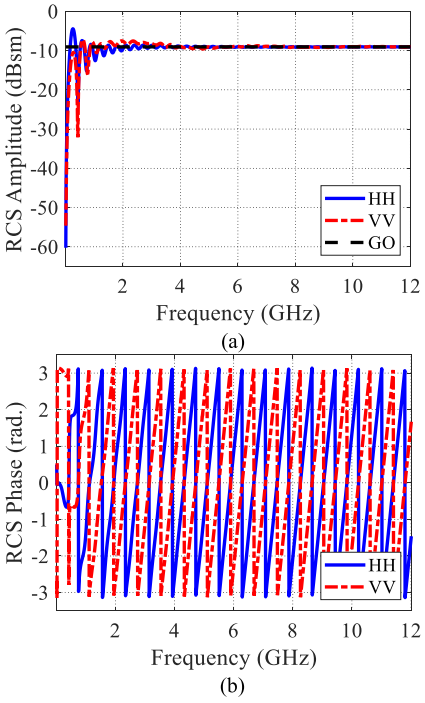

Fig. 3. Backscattering RCS versus frequency of a 15-in SEC calibrator. (a) RCS amplitude. (b) RCS phase.

corresponding with the scattering mechanism of the double-curved surface. The amplitudes for all the other SCs attenuate as the frequency increases. A more detailed analysis of the frequency-dispersive SCs is given as follows.

1) Surface Wave Component: It is noted that, when an EM field illuminates on a metal surface, surface waves are

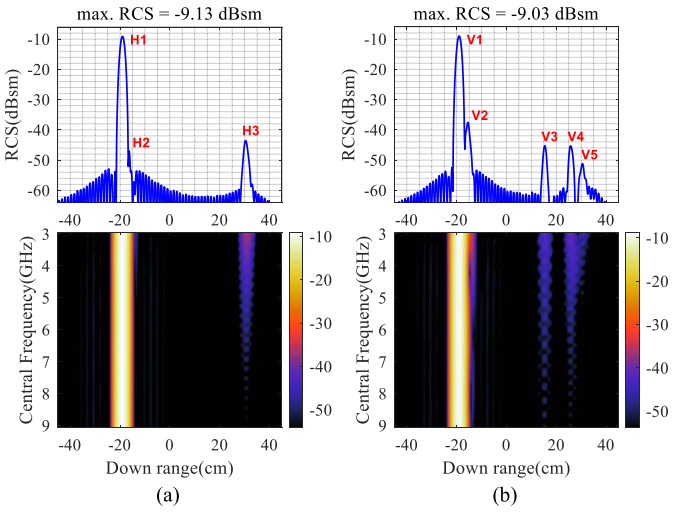

Fig. 4. TFRs of HRRPs for (a) HH polarization and (b) VV polarization.

launched only when the incident electric field has components perpendicular or parallel to the surface in the plane of incidence, which is defined by the surface normal and the EM wave direction of incidence [23]. For HH polarization, because only the side of the ellipsoid meets with the condition of exciting surface waves, there is only one creeping wave component, i.e., H3. On the other hand, for VV polarization, the upper and the lower plate surfaces as well as the side face of the calibrator all meet with the condition, resulting in three surface wave SCs, i.e., V3–V5. It is also worth noting that the SEC calibrator for VV polarization as in Fig. 4(b) has two fewer surface wave SCs than an SCC as analyzed in [9].

2) Second-Order Diffraction Wave Component: The diffraction wave of the SEC calibrator is excited by the second-order differential discontinuities. According to the physical theory of diffraction (PTD) [24], the diffraction wave makes significant contributions to backscattering when the incident electric field has a component perpendicular to the plane formed by the discontinuous edge and the EM wave direction of incidence. As a result, the diffraction wave V2 in VV polarization is much stronger than H2 in HH polarization.

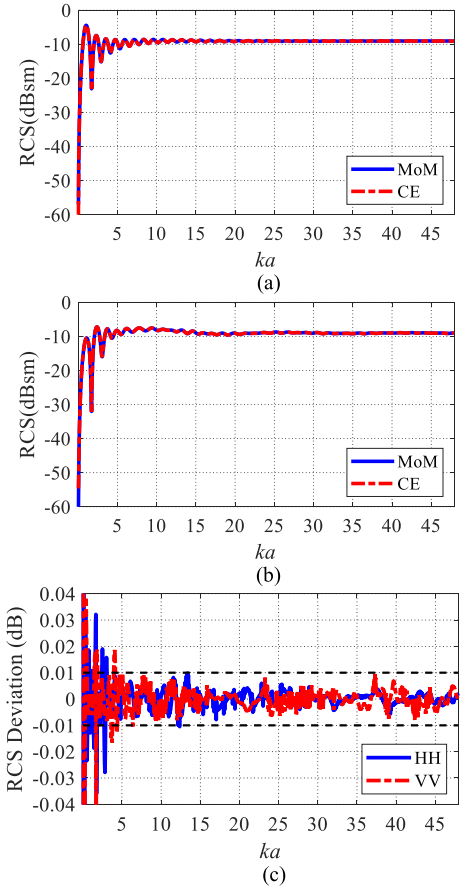

Fig. 5. Comparison of the CE model and MoM data for a 15-in SEC calibrator. (a) HH polarization. (b) VV polarization. (c) RCS deviation.

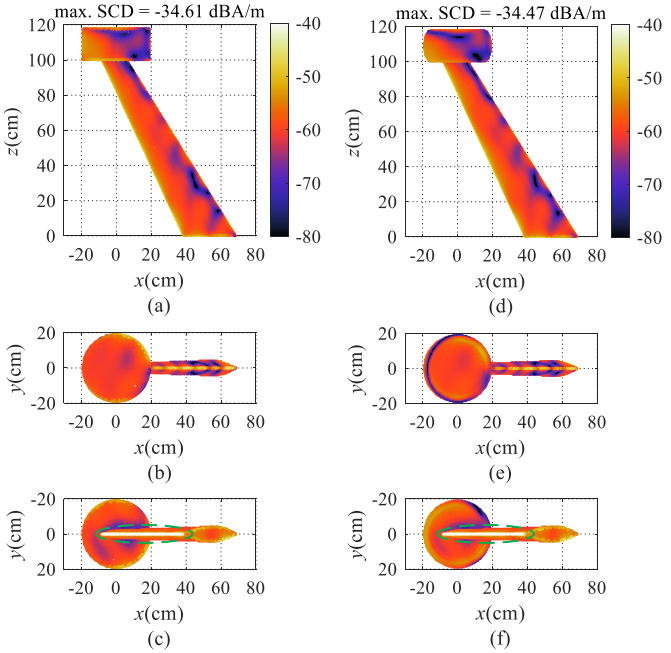

Fig. 6. Surface current distribution signature. (a) Side, (b) top, and (c) bottom view of SCC-pylon. (d) Side, (e) top, and (f) bottom view of SEC-pylon.

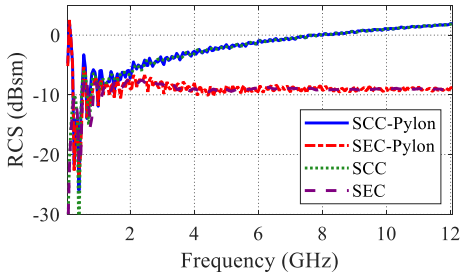

Fig. 7. RCS amplitude of calibrators alone and calibrator-pylon assemblies.

C. Parametric Representation of the Theoretical RCS

According to the EM scaling principles, for a set of ECs with a specified DHWR, the RCS normalized by the GO component only depends on the electric dimension, i.e., ka, where k is the radar wavenumber and a is the radius of the calibrator. According to [9], a CE-model-based calculation approach for the theoretical RCS of the SEC calibrator is established. A comparison of the MoM data and the CE model prediction data over a frequency of 0.01–12 GHz is presented in Fig. 5. It is seen that, for $ka \geqq 5$, the maximal deviations of the CE model prediction from the MoM data are within ± 0.01 dB for both polarizations, satisfying the requirements for almost all RCS calibration applications. The MATLAB code for the complex RCS calculating of a set of scaled SEC calibrators with DHWR = 15:7:1.5 is available via email to the authors.

III. Characterization of CPI

When the calibrator is mounted on a low RCS metal pylon, the CPI can be an important source of uncertainty in RCS measurement, especially for VV polarization [25]–[27]. The absolute error of the measured RCS caused by CPI is defined as (in m^2)

$$\varepsilon_{\mathrm{CPI}}(f) = \left| \sqrt{\sigma_{\mathrm{cp}}(f)} - \sqrt{\sigma_{\mathrm{c}}(f)} \right|^2 \tag{3}$$

where $\sqrt{\sigma_{\mathrm{c}}(f)}$ and $\sqrt{\sigma_{\mathrm{cp}}(f)}$ denote the scattering functions of the calibrator alone the calibrator-pylon assembly, respectively.

Fig. 6 shows the average surface current distributions of calibrator-pylon assemblies at 1 GHz for VV polarization calculated using MoM by FEKO software. It can be seen from Fig. 6 that for the two calibrator-pylon assemblies, the surface currents are both significant on the leading edge of the pylon, resulting in the excitation of surface waves in the same mechanism. The induced currents in turn create an accumulation of charges at the termination of the pylon. Then the radiation of the charges results in significant CPI.

The RCS versus frequency for VV polarization of the calibrators alone and calibrator-pylon assemblies from 50 MHz to 12.05 GHz with a step of 50 MHz is calculated using MoM, as illustrated in Fig. 7, where the RCS of calibrator-pylon assemblies includes the scattered field from the calibrator, the pylon, and the interactions. Consequently, the error caused by interactions cannot be calculated directly using (3). To exactly analyze the RCS error caused by CPI, the SCs of the pylon itself must be removed. In this article, CE model representation is used to extract these SCs [28], [29].

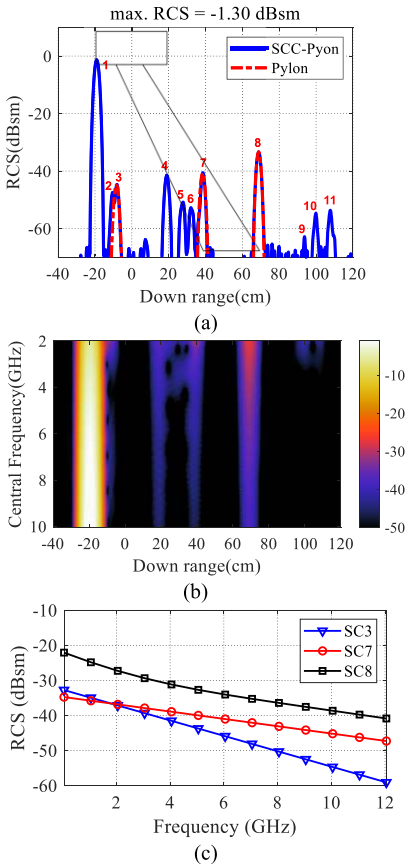

Fig. 8. HRRP and TFR of SCC-pylon for VV polarization. (a) HRRP. (b) TFR. (c) Extracted pylon SCs.

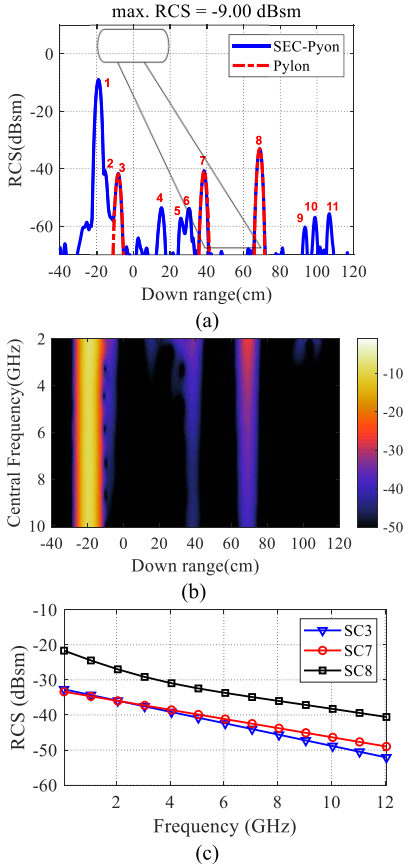

Fig. 9. HRRP and TFR of SEC-pylon for VV polarization. (a) HRRP. (b) TFR. (c) Extracted pylon SCs.

The CE model of radar target scattering function is

$$\sqrt{\sigma(f)} = \sum_{i=1}^{M} a_i e^{-\left(\alpha_i + \mathrm{j}\frac{4\pi r_i}{c}\right) f} \tag{4}$$

where M is the model order or the number of scattering components, a_i, α_i, and r_i are the complex amplitude, the frequency dispersion factor, and the distance from the target reference center of the ith SC, respectively, which can be estimated by the state space approach (SSA) [30], and f is the radar frequency vector.

Assuming that the kth SC can be reconstructed by the mth to nth scattering components, the scattering function of the kth SC can be written as

$$\sqrt{\sigma_k(f)} = \sum_{i=m}^{n} a_i e^{-\left(\alpha_i + \mathrm{j}\frac{4\pi r_i}{c}\right) f} \tag{5}$$

where m and n can be estimated in the HRRP.

The 1-D HRRP, TFR, and extracted SCs of the pylon are illustrated in Fig. 8 for SCC-pylon and Fig. 9 for SEC-pylon, respectively. According to the matching correlation between the geometry and HRRP, SC3, SC7, and SC8 are belonging to the pylon. As it can be seen from the RCS characteristics in Figs. 8(c) and 9(c), SC3 and SC7 are caused by tip diffraction, while SC8 is caused by the traveling wave. SC8 is the strongest among the three SCs because of the accumulation of charges corresponding to the previous analysis in Fig. 6.

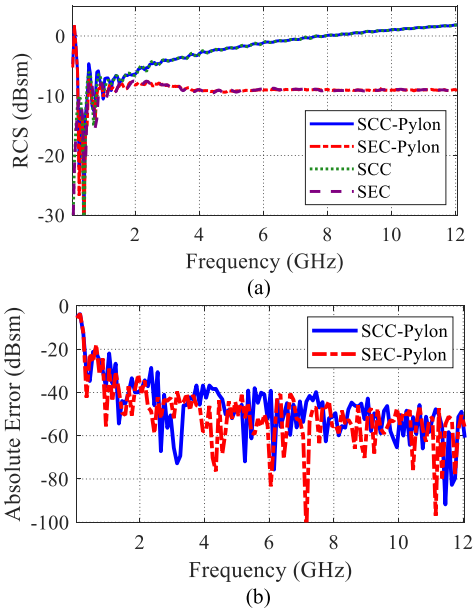

Fig. 10. Influence of the CPI after removing the SCs of the pylon. (a) RCS of calibrators and calibrator-pylon assemblies. (b) Absolute error caused by CPI.

After subtracting SCs of the pylon, the RCS of calibrator-pylon assemblies is shown in Fig. 10(a), where the RCS curves of

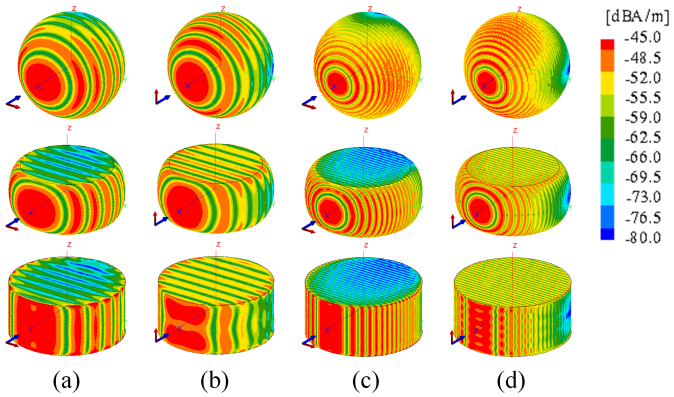

Fig. 11. Instantaneous surface current distribution of calibrators at (a) 3 GHz for HH and (b) VV polarizations, and (c) 10 GHz for HH and (d) VV polarizations.

the calibrators are also plotted for comparison. The absolute RCS error caused by CPI is shown in Fig. 10(b).

It is seen from Fig. 10(b) that for the SCC and SEC calibrators in the same diameter, the RCS errors caused by CPI of the two calibrator-pylon assemblies are at the same level and both decrease with frequency increases because the surface waves attenuate while specular reflection components of the calibrators dominate in the total backscattered field.

IV. Angle-Sensitive RCS Characteristics

The angular invariance of the RCS is one of the most important characteristics of the calibrator. A comparative study of the angle-sensitive RCS characteristics for both SCC and SEC calibrators is executed in this section.

A. Qualitative Analysis From Surface Current Distributions

It is well known that a metal sphere is an isotropic electric conductor, whose RCS is insensitive to the angle of the radar LOS. For qualitative analysis, the instantaneous surface current distributions of the sphere, SEC, and SCC are calculated using MoM by FEKO software, as illustrated in Fig. 11. The diameters of the three calibrators are all 15 in. For the SEC, the surface current distribution is quite similar to that of the sphere in all azimuth angles and a certain range of elevation angles, demonstrating that the RCS of the SEC is insensitive among that angular range. On the other hand, for the SCC, the surface current distribution is quite different in elevation, indicating that the RCS is sensitive to the elevation angle. With the increase in frequency, the isotropic characteristics of the elevation angle of the SEC and the anisotropic characteristic of the SCC become more distinctive.

B. Monostatic Cases

1) Elevation Angular Sensitivity: In the monostatic case, we discuss the RCS characteristics varying with elevation and roll angles. The incident EM wave with an elevation angle θ is shown in Fig. 12.

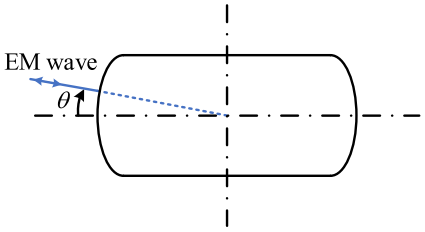

Fig. 12. Elevation angle of incident EM wave in monostatic measurement.

The RCS deviation caused by the elevation angle θ is defined as

$$\delta_{\text{elev}}(\theta) = \frac{\sigma(\theta)}{\sigma(0)}. \tag{6}$$

According to the GO theory, for the SCC calibrator, when θ is small, the RCS versus elevation angle can be expressed as [2]

$$\sigma_{\text{GO}}^{\text{SCC}}(\theta) = \frac{kdh^2}{2}\left[\cos\theta\frac{\sin(kh\sin\theta)}{kh\sin\theta}\right]^2 \tag{7}$$

where $k = 2\pi/\lambda$ denotes the wavenumber and d and h are the diameter and height of the SCC, respectively.

The RCS deviation of the SCC calibrator is

$$\delta_{\text{elev}}^{\text{SCC}}(\theta) = \left[\frac{\cos\theta\sin(kh\sin\theta)}{kh\sin\theta}\right]^2. \tag{8}$$

For convenience, (8) can be approximated by Taylor series expansion, given as

$$\delta_{\text{elev}}^{\text{SCC}}(\theta) \approx \left[1 - \frac{(kh\theta)^2}{6}\right]^2. \tag{9}$$

On the other hand, for the SEC, the RCS deviation based on GO theory can be derived from (54) in Appendix B as

$$\delta_{\text{elev}}^{\text{SEC}}(\theta) = \frac{8w^3\left[(d-2w)\sqrt{(h\sin\theta)^2+(2w\cos\theta)^2}+4w^2\cos\theta\right]}{d\cos\theta\left[(h\sin\theta)^2+(2w\cos\theta)^2\right]^2}. \tag{10}$$

From (B8) in Appendix B, the following equation can be approximated as

$$\delta_{\text{elev}}^{\text{SEC}}(\theta) \approx \left\{1 - \left[(h/2w)^2 - 1\right]\theta^2\right\}^2 \tag{11}$$

where w should also be limited to $w > \lambda/8$.

From (9) and (11), it is found that the RCS deviation for the CC calibrator is related to the electrical dimension along the height kh, while that for the EC calibrator is dependent on the height-to-width ratio, that is, h/w.

The RCS deviations of the two 15-in SCC and SEC calibrators versus elevation angles from 0° to 10° with a step of 0.1° are illustrated in Fig. 13, where the results are calculated using MoM and GO formulas as in (8) and (10). For the SCC calibrator, when the elevation angle changes by 2°, the RCS deviation is about −0.23 dB at 3 GHz frequency and −2.60 dB at 10 GHz frequency. The higher the frequency, the greater the RCS deviation is, which is coincident with the analysis as in (9). On the other hand, for the SEC calibrator, when the

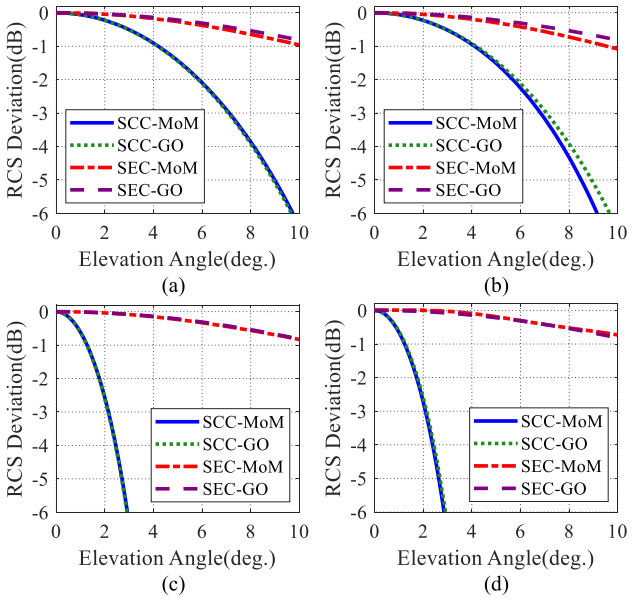

Fig. 13. RCS deviation versus elevation angle at (a) 3 GHz for HH and (b) VV polarizations, and (c) 10 GHz for HH and (d) VV polarizations.

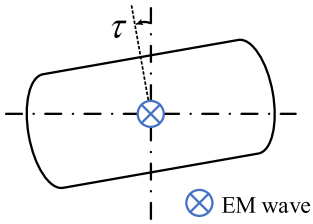

Fig. 14. Calibrator with a roll angle in monostatic measurement.

elevation angle changes by 2°, the RCS deviation is less than −0.1 dB at both 3 and 10 GHz frequencies, which is almost independent of frequency, coinciding with the conclusion as in (11).

2) Roll Angular Sensitivity: For a polarization-sensitive calibrator, roll angle might cause a depolarization effect. The calibrator with a roll angle τ is shown in Fig. 14. Since the roll angle caused by the imperfect installation is usually small, a 10° roll angle is given as an example. The RCS amplitudes versus frequency for HH and VV polarizations of SCC and SEC calibrators are calculated using MoM in Fig. 15.

The depolarization effect of both SCC and SEC calibrators caused by the roll angle is due to the difference in the surface waves for HH and VV polarizations. It is seen from Fig. 15 that for a roll angle as large as 10°, no obvious deviation on the backscattered field for both SCC and SEC calibrators.

C. Bistatic Cases

According to Kell's [31] SC-based monostatic-to-bistatic equivalence theorem (MBET), the relation of bistatic and

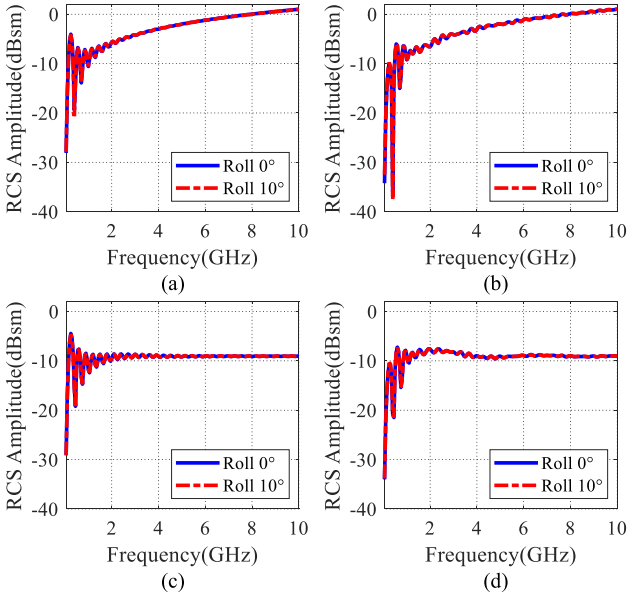

Fig. 15. Backscattering RCS with a roll angle of calibrators. (a) HH and (b) VV polarizations for SCC. (c) HH and (d) VV polarizations for SEC.

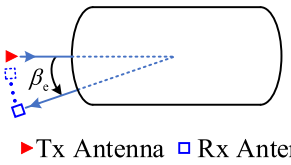

Fig. 16. Transceiver path of bistatic elevation angle geometry.

monostatic for RCS solutions can be expressed as

$$\sigma_{\mathrm{Bi}}(f = f_0, \alpha = \beta_0) = \sigma_{\mathrm{Mono}}\left(f = f_0 \cos\frac{\beta_0}{2}, \alpha = \frac{\beta_0}{2}\right) \tag{12}$$

where σ_{Bi} and σ_{Mono} are the bistatic and monostatic RCS solutions, α is the receiver orientation angle, f is the radar frequency, and β_0 and f_0 are the bistatic angle and frequency, respectively.

The RCS deviation caused by the bistatic angle β is defined as

$$\delta_{\mathrm{Bi}}(\beta) = \frac{\sigma_{\mathrm{Bi}}(f, \beta)}{\sigma_{\mathrm{Mono}}(f, 0)}. \tag{13}$$

The RCS characteristics on bistatic angles along elevation and azimuth are discussed in the following.

1) Bistatic in Elevation: A satisfactory property in the elevation bistatic case is highly required in advanced RCS test fields such as outdoor GPR and RCS ranges using antenna arrays.

Fig. 16 illustrates the bistatic case of an elevation angle β_e with the transmitting (Tx) and receiving (Rx) antennas.

According to (12), the RCS of bistatic GO (BGO) for SCC and SEC calibrators can be expressed, respectively, as

$$\sigma_{\mathrm{BGO}}^{\mathrm{SCC}}(\beta_e) = \frac{kdh^2}{2}\cos\left(\frac{\beta_e}{2}\right)\left\{\cos\left(\frac{\beta_e}{2}\right)\frac{\sin[kh\sin(\beta_e/2)]}{kh\sin(\beta_e/2)}\right\}^2 \tag{14}$$

and (15), as shown at the bottom of the next page.

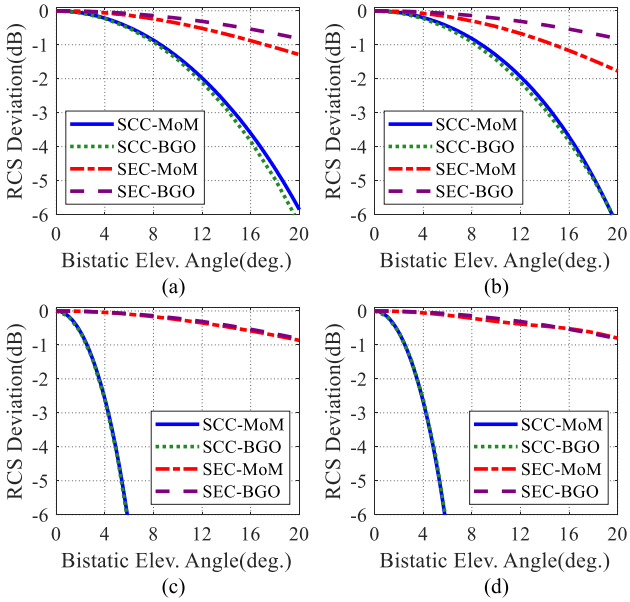

Fig. 17. RCS deviation versus bistatic elevation angle at (a) 3 GHz for HH and (b) VV polarizations, and (c) 10 GHz for HH and (d) VV polarizations.

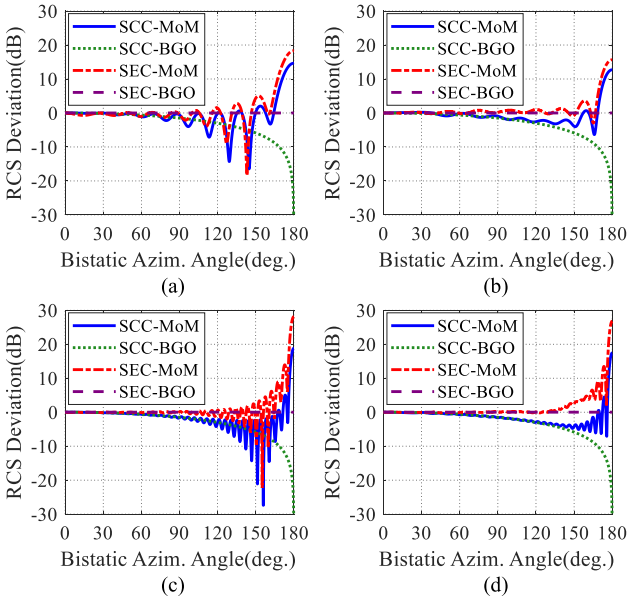

Fig. 19. RCS deviation versus bistatic azimuth angle at (a) 3 GHz for HH and (b) VV polarizations, and (c) 10 GHz for HH and (d) VV polarizations.

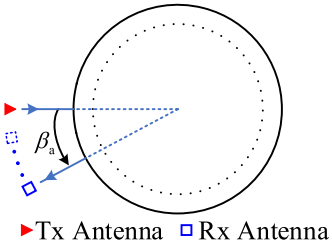

Fig. 18. Transceiver path of bistatic azimuth angle geometry.

The RCS deviations of the two 15-in calibrators versus bistatic elevation angles from 0° to 20° with a step of 0.1° are illustrated in Fig. 17(a)–(d). For the SCC calibrator, when the bistatic elevation angle changes by 4°, the RCS deviation is about −0.23 dB at 3 GHz frequency and −2.60 dB at 10 GHz frequency. On the other hand, for the SEC calibrator, when the bistatic angle changes by 4°, the RCS deviation is within −0.1 dB at both 3 and 10 GHz frequencies.

2) Bistatic in Azimuth: Whether or not a calibrator can be used for bistatic RCS measurement depends on its azimuthal bistatic RCS characteristics. The bistatic case of an azimuth angle β_a for a calibrator is shown in Fig. 18.

According to (12), the RCS of BGO in the case of the SCC and SEC calibrators can be expressed, respectively, as

$$\sigma_{\mathrm{BPO}}^{\mathrm{SCC}}(\beta_a) = \frac{kdh^2}{2}\cos\left(\frac{\beta_a}{2}\right) \tag{16}$$

and

$$\sigma_{\mathrm{BPO}}^{\mathrm{SEC}}(\beta_a) = \frac{\pi dh^2}{8w}. \tag{17}$$

The RCS deviations of both SCC and SEC calibrators versus bistatic azimuth angles from 0° to 180° with a step of 0.1° are illustrated in Fig. 19.

It is seen from Fig. 19 that as the azimuthal bistatic angle increases, the deviation of the SCC also increases because of its bistatic dispersion which is essentially the frequency-dispersive effect. On the other hand, for the SEC calibrator, its RCS remains stable as the bistatic angle increases with less than ±0.5 dB of RCS deviation within 100° bistatic azimuth angle at 10 GHz, demonstrating its promising bistatic RCS characteristics.

V. Characterization of Calibration Uncertainty in GPR

A. Ground-Plane Range

The geometry of a GPR is illustrated in Fig. 20. The total field from multipath echoes is expressed as [2]

$$E = E_0\left[e^{-\mathrm{j}2kD} + 2\rho e^{-\mathrm{j}k(D+I)} + \rho^2 e^{-\mathrm{j}2kI}\right] \tag{18}$$

where E_0 represents the incident field, $k = 2\pi/\lambda$ denotes the wavenumber, ρ refers to the ground reflection coefficient, and D and I are the one-way distance of direct and indirect paths, respectively.

$$\sigma_{\mathrm{BGO}}^{\mathrm{SEC}}(\beta_e) = \frac{\pi h^2 w^2\left[(d-2w)\sqrt{\left(h\sin\frac{\beta_e}{2}\right)^2 + \left(2w\cos\frac{\beta_e}{2}\right)^2} + 4w^2\cos\frac{\beta_e}{2}\right]}{\cos\frac{\beta_e}{2}\left[\left(h\sin\frac{\beta_e}{2}\right)^2 + \left(2w\cos\frac{\beta_e}{2}\right)^2\right]^2}. \tag{15}$$

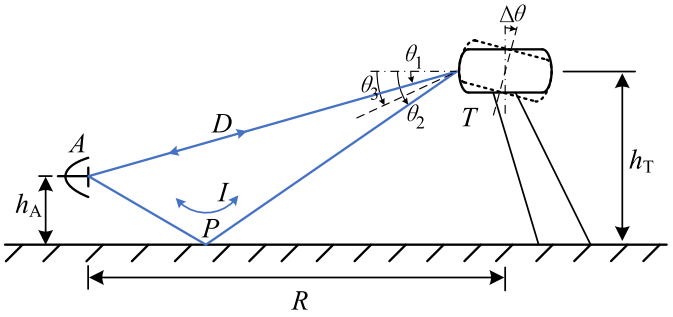

Fig. 20. Multipath scattering for RCS measurement in GPR.

Assuming that the ground plane is perfectly conducting, the reflection coefficient is equal to −1. The GPR produces a 12 dB theoretical gain when compared to a free-space test range when the locations of the antenna and target satisfy the relation as

$$h_{\mathrm{A}} \cdot h_{\mathrm{T}} = \frac{\lambda}{4} \cdot R \tag{19}$$

where h_{A} and h_{T} stand for the heights of antenna and target, respectively, and R is the measurement distance.

In GPR, because of the ground-plane effect, there are four distinct propagation paths, resulting in elevation geometries for both calibrator and target measurement. The direct path *ATA* with an elevation angle θ_1 and the double ground reflection path *APTPA* with an elevation angle of θ_2. On the other hand, the single ground reflection paths *ATPA* and *APTA* with a bistatic elevation angle, which can be treated as a monostatic case at the bisector denoted as θ_3 according to MBET [31].

For an angle-sensitive calibrator, the field gain factor (FGF) varying with incident angle is defined as

$$g(\theta) = \sqrt{\frac{\sigma(\theta)}{\sigma(0)}}. \tag{20}$$

According to Fig. 20, the three incident angles for different paths can be expressed as

$$\theta_1 = \arctan[(h_{\mathrm{T}} - h_{\mathrm{A}})/R] \approx (h_{\mathrm{T}} - h_{\mathrm{A}})/R \tag{21a}$$

$$\theta_2 = \arctan[(h_{\mathrm{T}} + h_{\mathrm{A}})/R] \approx (h_{\mathrm{T}} + h_{\mathrm{A}})/R \tag{21b}$$

$$\theta_3 = (\theta_1 + \theta_2)/2 \approx h_{\mathrm{T}}/R. \tag{21c}$$

Combining (18)–(20), the total field can be expressed as a function of the incident angles as

$$|E| = |E_0[g(\theta_1) + 2g(\theta_3) + g(\theta_2)]|. \tag{22}$$

To characterize the calibration error, we define the power gain factor (PGF) K as the ratio of the scattered power to incident wave power, that is,

$$K = \left|\frac{E}{E_0}\right|^2. \tag{23}$$

The multipath propagation in GPR means that, even if the calibrator is perfectly mounted on a pylon, there are still different incident angles corresponding to different propagation paths, resulting in an incident error. On the other hand, when with an imperfect mount where the calibrator has a small tilt angle, tilt error occurs in addition to incident error.

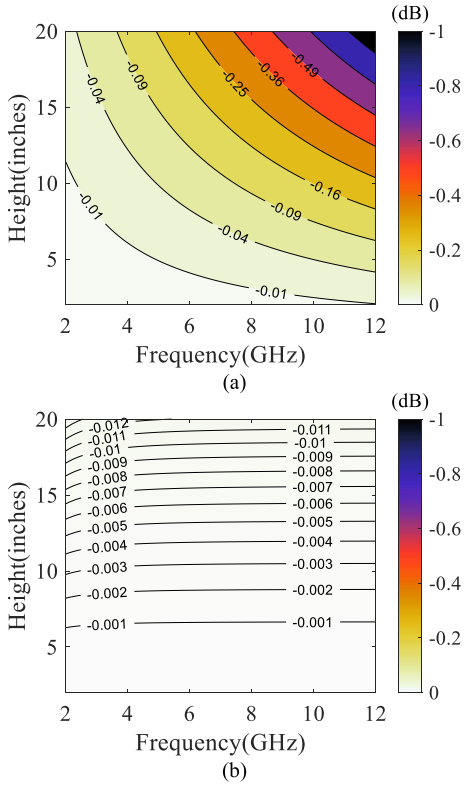

Fig. 21. Incident error versus frequency and height. (a) Circular and (b) EC calibrator.

B. Incident Error

Considering an isotropic calibrator whose FGF $g(\theta) \equiv 1$, we define the incident error as the ratio of PGF of the calibrator under test K_{T} to that of the isotropic calibrator K_{iso}

$$\varepsilon_{\mathrm{inc}} = \frac{K_{\mathrm{T}}(\theta)}{K_{\mathrm{iso}}(\theta)}. \tag{24}$$

According to (22) and (23), we have

$$\varepsilon_{\mathrm{inc}} = \left|\frac{g(\theta_1) + 2g(\theta_3) + g(\theta_2)}{4}\right|^2. \tag{25}$$

For the SCC and SEC calibrators, the FGFs are, respectively,

$$g_{\mathrm{SCC}}(\theta) = \left|\cos\theta \frac{\sin(kh\sin\theta)}{kh\sin\theta}\right| \tag{26}$$

and

$$g_{\mathrm{SEC}}(\theta) = \left\{\frac{8w^3\left[(d-2w)\sqrt{(h\sin\theta)^2 + (2w\cos\theta)^2} + 4w^2\cos\theta\right]}{d\cos\theta\left[(h\sin\theta)^2 + (2w\cos\theta)^2\right]^2}\right\}^{\frac{1}{2}}. \tag{27}$$

As an illustration of the incident error, numerical calculations for both CC and EC calibrators are shown in Fig. 21(a) and (b). The two kinds of calibrators are both fixed 15-in diameter. The width of EC is fixed at 1.5 in. The heights of the calibrators vary from 2 to 20 in, meaning that the DHR of the two calibrators varies from 7.5 to 0.75. The

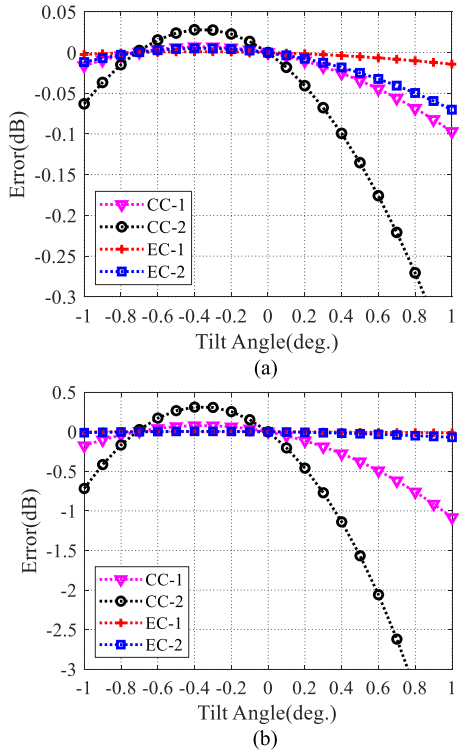

Fig. 22. Tilt error versus tilt angle at (a) 3 GHz and (b) 10 GHz frequencies.

radar frequency varies from 2 to 12 GHz. The calibrators are supposed to be mounted on a 10-m high pylon with a radar distance of 1600 m.

For further analysis, using Taylor series expansion and retaining the second-order terms, the FGFs for the two calibrators are approximated as

$$g_{\mathrm{SCC}}(\theta) \approx 1 - \frac{(kh\theta)^2}{6} \tag{28}$$

and

$$g_{\mathrm{SEC}}(\theta) \approx 1 - \left[(h/2w)^2 - 1\right]\theta^2 \tag{29}$$

where a detailed derivation of $g_{\mathrm{SEC}}(\theta)$ can be found in (B9).

From (21) and noting that $h_{\mathrm{t}} \gg \lambda$, the incident errors can be approximated, respectively, as

$$\varepsilon_{\mathrm{inc}}^{\mathrm{SCC}} \approx \left\{1 - \frac{(kh)^2}{6}\left(\frac{h_T}{R}\right)^2\right\}^2 \tag{30}$$

and

$$\varepsilon_{\mathrm{inc}}^{\mathrm{SEC}} \approx \left\{1 - \left[\left(\frac{h}{2w}\right)^2 - 1\right]\left(\frac{h_{\mathrm{T}}}{R}\right)^2\right\}^2 \tag{31}$$

for $w > \lambda/8$.

According to (30) and (31), the incident error of SCC and SEC increases with $(kh)^2/6$ and $(h/2w)^2$, respectively, verified in Fig. 21. When h is equal to $2w$, the SEC becomes a spheroidal cylinder with an incident error equal to 0 to a certain range of elevation angle.

TABLE III
SIZES OF CALIBRATORS FOR TILT ERROR CALCULATION

Calibrator	Diameter (inches)	Height (inches)	Width (inches)
CC-1 (SCC)	15	7	—
CC-2	15	14	—
EC-1 (SEC)	15	7	1.5
EC-2	15	14	1.5

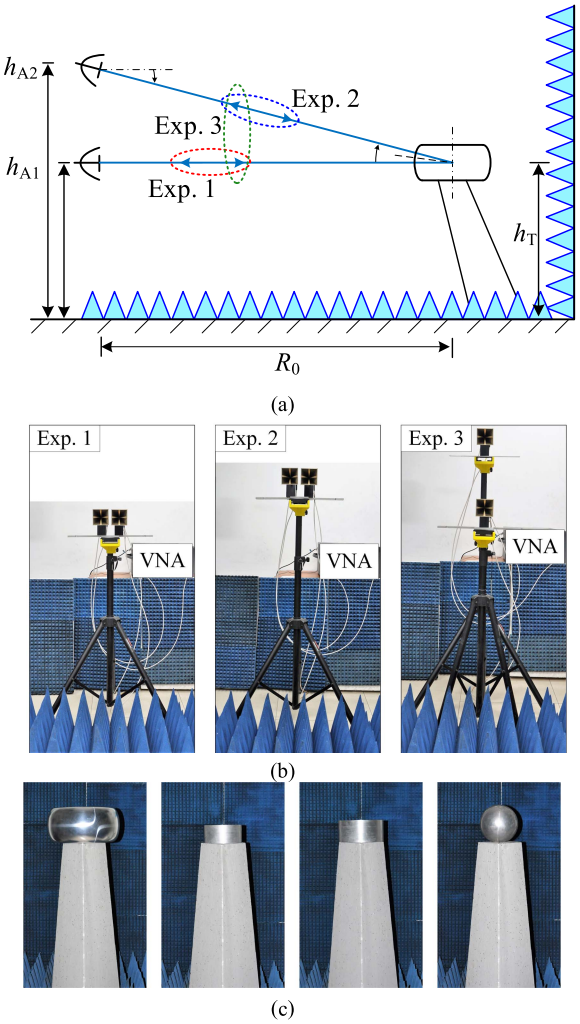

Fig. 23. RCS measurement experiments in an indoor test range. (a) Scattering paths of the three experiments. (b) Measurement systems. (c) Calibrators on a foam column under test.

C. Tilt Error

The calibrator mounted with a small tilt angle $\Delta\theta$ is illustrated in Fig. 20 (although it is enlarged here). We define the tilt angle $\Delta\theta$ as an elevation angle for $\Delta\theta > 0$ and a depression angle for $\Delta\theta < 0$.

Corresponding to (21), with a tilt angle $\Delta\theta$, the incident angles are, respectively,

$$\theta_1 = \theta_1 + \Delta\theta \tag{32a}$$

$$\theta_2 = \theta_2 + \Delta\theta \tag{32b}$$

$$\theta_3 = (\theta_1 + \theta_2)/2 + \Delta\theta. \tag{32c}$$

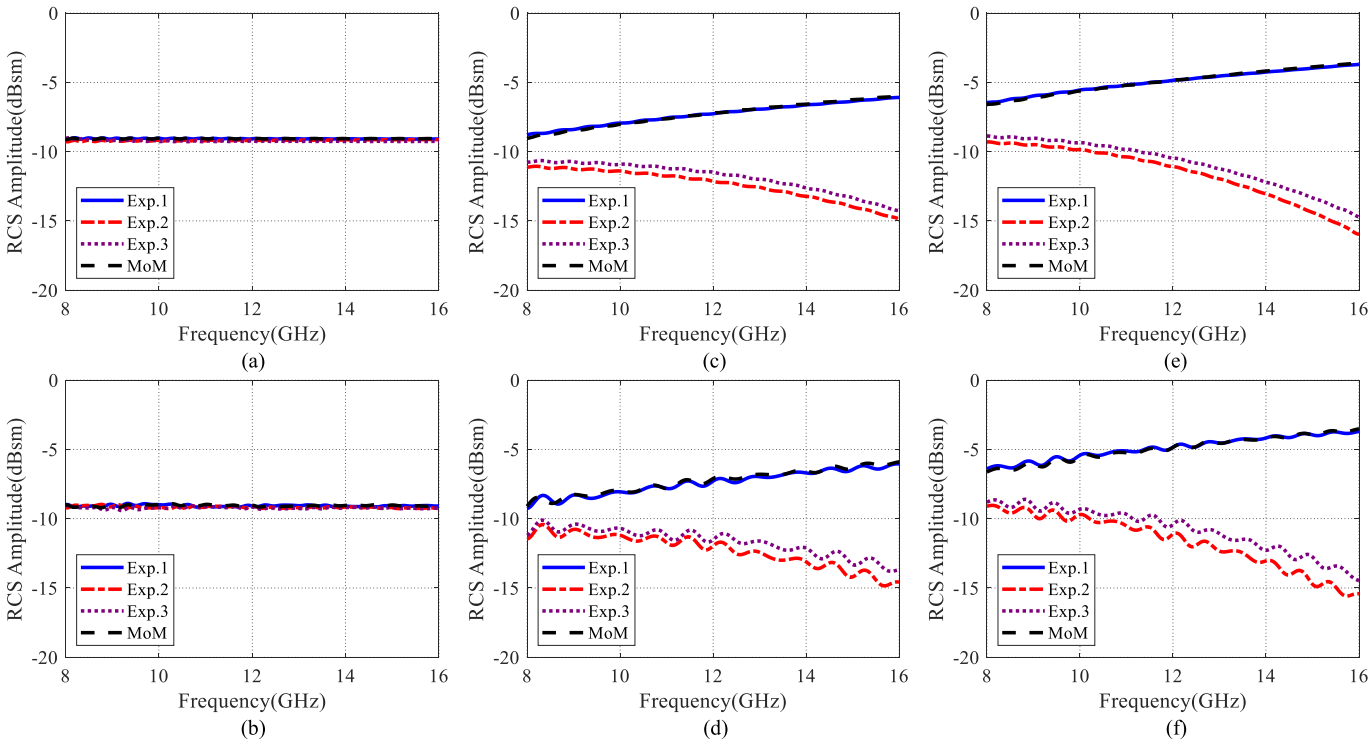

Fig. 24. RCS amplitude of experimental and theoretical data after calibration. (a) HH and (b) VV polarizations for the SEC calibrator. (c) HH and (d) VV polarizations for the M750 cylinder. (e) HH and (f) VV polarizations for the L900 cylinder.

The tilt error is defined as the ratio of PGF of the calibrator with a tilt angle $K_{\mathrm{T}}(\Delta\theta)$ to a perfectly no tilt case $K_{\mathrm{T}}(0)$

$$\varepsilon_{\mathrm{tilt}} = \frac{K_{\mathrm{T}}(\Delta\theta)}{K_{\mathrm{T}}(0)}. \tag{33}$$

According to (22), the tilt error is represented as

$$\varepsilon_{\mathrm{tilt}} = \left| \frac{g(\theta_1+\Delta\theta) + 2g(\theta_3+\Delta\theta) + g(\theta_2+\Delta\theta)}{g(\theta_1) + 2g(\theta_3) + g(\theta_2)} \right|^2. \tag{34}$$

For example, Fig. 22(a) and (b) shows the numerical calculation of tilt error for different sized CCs and ECs at 3 and 10 GHz frequencies, respectively. The sizes of the calibrators under calculation are listed in Table III.

Using the small-angle approximation similar to (28) and (29), we have

$$g_{\mathrm{SCC}}(\theta+\Delta\theta) \approx g_{\mathrm{SCC}}(\theta) - \frac{(kh)^2\theta\Delta\theta}{3} - \frac{(kh\Delta\theta)^2}{6} \tag{35}$$

$$g_{\mathrm{SEC}}(\theta+\Delta\theta) \approx g_{\mathrm{SEC}}(\theta) - \left[\left(\frac{h}{2w}\right)^2 - 1\right]\Delta\theta(\theta+\Delta\theta). \tag{36}$$

The tilt errors of the two calibrators can be approximated as

$$\varepsilon_{\mathrm{tilt}}^{\mathrm{SCC}} \approx \left[1 - \frac{(kh)^2}{6}\Delta\theta\left(\Delta\theta + \frac{2h_{\mathrm{T}}}{R}\right)\right]^2 \tag{37}$$

$$\varepsilon_{\mathrm{tilt}}^{\mathrm{SEC}} \approx \left\{1 - \left[\left(\frac{h}{2w}\right)^2 - 1\right]\Delta\theta\left(\Delta\theta + \frac{2h_{\mathrm{T}}}{R}\right)\right\}^2 \tag{38}$$

for $w > \lambda/8$.

In conclusion, the calibration errors for SCC are related to $(kh)^2/6$, while for SEC, it is dependent on $(h/2w)^2$. As a consequence, for reduced RCS calibration error in GPR, the CC calibrator must be a "squat" design, while the EC calibrator can be properly designed of DHWR, not necessarily be "squat."

VI. Experimental Results

In order to compare the sensitivity to elevation angle in both monostatic and bistatic cases, three experiments in an indoor RCS measurement range are performed, that is, 1) quasi-monostatic measurement with normal incidence; 2) quasi-monostatic measurement with an elevation angle; and 3) bistatic measurement to simulate an antenna array. The configuration of the measurement experiments is shown in Fig. 23. The measurement systems consist of two wideband dual-polarized horn antennas and a vector network analyzer (VNA) are illustrated in Fig. 23(b). The size of the two antennas is 85 mm and the distance between them in quasi-monostatic cases is 20 mm. The four calibrators on a foam column under test are, respectively, an SEC sized 15-in diameter, an M750 [9] SCC sized 7.5-in diameter, an L900 SCC sized 9-in diameter, and a calibration sphere sized 200-mm diameter, as seen in Fig. 23(c). The measurement parameters are listed in Table IV. It is noted that the elevation angle in Experiment 2 is about 4°, while the bistatic angle in Experiment 3 is about 8°.

Fig. 24 illustrates the experimental and theoretical RCS of the calibrators, where the blue solid, red dashed-dotted, purple dotted, and black dashed lines denote, respectively, the

TABLE IV
MEASUREMENT PARAMETERS

Parameters	Exp. 1	Exp. 2	Exp. 3
Tx antenna height(m)	1.20	1.58	1.20
Rx antenna height(m)	1.20	1.58	1.96
Measurement distance(m)		5.40	
Radar frequency(GHz)		8.0–16.0	
Frequency sampling points		801	

measurement data in Experiments 1–3 and the backscattering data calculated using MoM.

From Fig. 24(a) and (b), it is found that the RCS of the SEC calibrator is actually insensitive to frequency and elevation angle, with the RCS error less than 0.1 dB in Experiments 2 and 3. On the other hand, it is seen from Fig. 24(c)–(f) that the RCS error of the SCCs varies obviously with frequency and dimension, that is, the electrical dimension, as analyzed in Section III. In addition, it is worth noting that the RCS error for SCCs in Experiment 3 is lower than that in Experiment 2, which is mostly because the bistatic effect leads to a lower frequency of $f\cdot\cos(\beta/2)$ than monostatic, with β being the bistatic angle. On the contrary, the RCS error of the SEC calibrator in Experiments 2 and 3 has little difference, as seen in Fig. 24(a) and (b). Thus, the RCS of the SEC calibrator is insensitive to the bistatic angle.

VII. CONCLUSION

A novel EC calibrator for RCS measurement is proposed and comprehensively characterized in this work. Except for its geometrical simplicity, the advantages of the proposed EC calibrator are as follows:

1) the RCS of the calibrator is insensitive to the elevation angle as well as the radar frequency, and the theoretical RCS can be calculated quickly and accurately using parametric representation;
2) the calibrator can be easily mounted on a low RCS pylon with negligible EM interaction;
3) the size and geometrical parameters can be well designed to balance the RCS level and the angular sensitivity to meet practical engineering requirements; and
4) for both monostatic and bistatic measurements, the expected calibration error is lower when the new calibrator is used instead of a CC.

In summary, theoretical analysis and experimental results demonstrate that the proposed EC calibrator can be a great candidate to replace the SCC for either indoor or outdoor uses, with special importance for outdoor GPRs or for RCS ranges where antenna arrays are used.

APPENDIX

A. GO Solution

The RCS of a double-curved surface at high frequency can be approximated based on GO theory as [19], [20]

$$\sigma_{\mathrm{GO}} = \pi\rho_1\rho_2 \tag{A1}$$

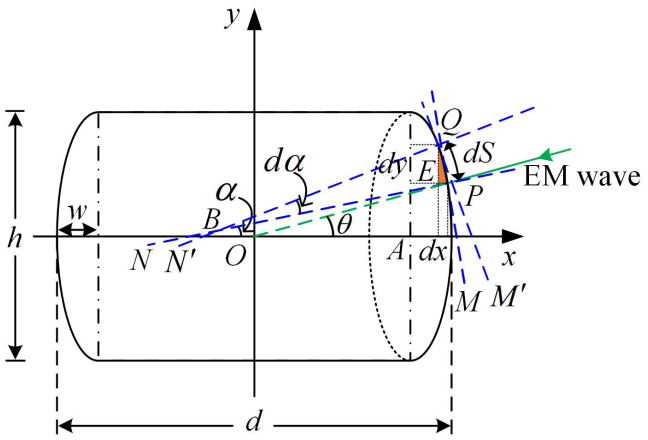

Fig. 25. Front cross section of the EC calibrator.

where ρ_1 and ρ_2 are the two principal curvature radii of the calibrator at the specular reflection point with ρ_1 and $\rho_2 \gg \lambda$, with λ being the radar wavelength. The specular reflection point is the point where the outer normal points to the radar LOS. The main curvature radii are the radii of curvature in two planes that contain the outer normal of the specular point and are perpendicular to each other. When the elevation angle θ that the radar LOS bias from broadside incidence is small, the two main curvature radii can be derived by differential geometry [21].

First, the curvature radius ρ_1 of the front cross section is derived as follows. Considering the geometric center of the calibrator as the phase reference center in RCS measurement, the Cartesian coordinate system xOy is established in Fig. 25. The incident EM wave PO intersects the front cross section at point P, with an incident angle θ. PM and PN are the tangent and normal lines at point P, respectively. $\angle\alpha$ is the angle between PN and the x-axis.

The elliptic equation centered on point A is

$$\frac{[x-(d/2-w)]^2}{w^2} + \frac{y^2}{(h/2)^2} = 1. \tag{A2}$$

Take the derivative of (40) with respect to x, we get

$$\frac{dy}{dx} = -\frac{(h/2)^2}{w^2}\cdot\frac{x-d/2+w}{y}. \tag{A3}$$

The slope of the tangent line PM can be expressed as

$$\frac{dy}{dx} = \tan\left(\frac{\pi}{2}+\alpha\right) = -\cot\alpha. \tag{A4}$$

From (41) and (42), we have

$$y = (x-d/2+w)\frac{(h/2)^2}{w^2}\tan\alpha. \tag{A5}$$

Substituting (43) into (40), we obtain

$$\frac{(x-d/2+w)^2}{w^2} + \frac{(x-d/2+w)^2(h/2)^2\tan^2\alpha}{w^4} = 1. \tag{A6}$$

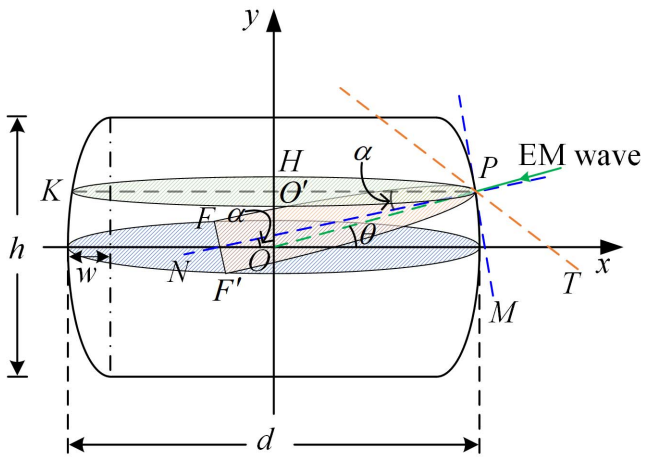

Fig. 26. Orthogonal plane of the EC calibrator.

Multiply both sides of (44) by $w^4\cos^2\alpha$ and after simplifying, we get

$$x=\frac{d}{2}-w+\frac{w^2\cos\alpha}{\left[(h/2)^2\sin^2\alpha+w^2\cos^2\alpha\right]^{1/2}}. \tag{A7}$$

Equation (45) is the abscissa of point P.

In Fig. 25, a differential arc dS is taken from P to Q, whose corresponding increment in the x-axis is dx, in the y-axis is dy, and the angle increment is dα. According to the definition of the curvature radius of a surface, the curvature radius ρ_1 at point P can be expressed as

$$\rho_1=\frac{dS}{d\alpha}. \tag{A8}$$

According to the differential triangle PEQ, we get

$$dS=-\frac{dx}{\sin\alpha} \tag{A9}$$

the minus sign in (A9) is because x decreases as angle α increases.

Take the derivative of (45) with respect to α, we can get

$$\frac{dx}{d\alpha}=\frac{-(h/2)^2w^2\sin\alpha}{\left[(h/2)^2\sin^2\alpha+w^2\cos^2\alpha\right]^{3/2}}. \tag{A10}$$

According to (46)–(48), the curvature radius ρ_1 can be derived as

$$\rho_1=\frac{(h/2)^2w^2}{\left[(h/2)^2\sin^2\alpha+w^2\cos^2\alpha\right]^{3/2}}. \tag{A11}$$

Second, the curvature radius ρ_2 of the orthogonal plane is derived as follows which is the plane PFF' in Fig. 26 containing the normal line PN and being perpendicular to the front cross section.

A plane PHK is established with O' as the center and parallel to the lower and upper flat planes of the calibrator. The plane PFF' and the plane PHK have a common tangent line PT. α is the angle between the two planes. According to Meusnier's theorem [21] in differential geometry, the relation between the two curvature radii ρ_2 of PFF' and ρ_{PHK} of PHK is

$$\rho_{PHK}=\rho_2\cos\alpha. \tag{A12}$$

It is seen that ρ_{PHK} is the absolute value of abscissa at point P, that is, $|x|$. According to (45), the curvature radius ρ_2 can be expressed as

$$\rho_2=\frac{(d/2-w)}{\cos\alpha}+\frac{w^2}{\left[(h/2)^2\sin^2\alpha+w^2\cos^2\alpha\right]^{1/2}}. \tag{A13}$$

When the incident angle is small, we have $\theta\approx\alpha$. As a result, the RCS of the EC at a higher frequency band can be expressed as

$$\sigma_{\mathrm{GO}}^{\mathrm{EC}}(\theta)=\frac{\pi h^2w^2\left[(d-2w)\sqrt{(h\sin\theta)^2+(2w\cos\theta)^2}+4w^2\cos\theta\right]}{\cos\theta\left[(h\sin\theta)^2+(2w\cos\theta)^2\right]^2}. \tag{A14}$$

In addition, considering the transition from double-curved surface to single-curved surface, the range of the parameter w is limited to

$$w>\lambda/8 \tag{A15}$$

where λ is the radar wavelength.

B. RCS Deviation Analysis of EC Calibrator

According to (52), the RCS deviation to the elevation angle of the EC calibrator is

$$\delta_{\mathrm{elev}}^{\mathrm{EC}}(\theta)=\frac{8w^3\left[(d-2w)\sqrt{(h\sin\theta)^2+(2w\cos\theta)^2}+4w^2\cos\theta\right]}{d\cos\theta\left[(h\sin\theta)^2+(2w\cos\theta)^2\right]^2}. \tag{B1}$$

Besides, the FGF of the EC calibrator defined in (20) is

$$g_{\mathrm{EC}}(\theta)=\left\{\frac{8w^3\left[(d-2w)\sqrt{(h\sin\theta)^2+(2w\cos\theta)^2}+4w^2\cos\theta\right]}{d\cos\theta\left[(h\sin\theta)^2+(2w\cos\theta)^2\right]^2}\right\}^{\frac{1}{2}}. \tag{B2}$$

In this article, we simplify the formula for the convenience of theoretical analysis. Considering when the incident elevation angle is quite small, that is, $\theta\ll 1$, we can make the following approximation:

$$\sqrt{(h/2)^2\sin^2\theta+w^2\cos^2\theta}\approx w\cos\theta. \tag{B3}$$

Then, (51) can be approximated as

$$\rho_2'=\frac{wd/2}{\left[(h/2)^2\sin^2\alpha+w^2\cos^2\alpha\right]^{1/2}}. \tag{B4}$$

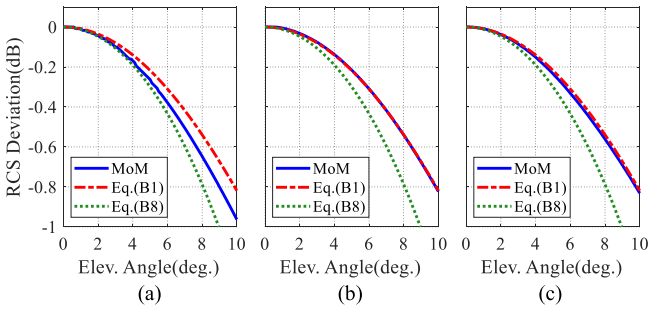

Fig. 27. RCS deviation calculated using MoM and GO formulas at (a) 3 GHz, (b) 6 GHz, and (c) 10 GHz frequencies.

As a result, the RCS of the EC can be derived from (49) and (57) as

$$\sigma'^{\mathrm{EC}}_{\mathrm{GO}}(\theta) = \frac{2\pi d h^2 w^3}{\left[(h\sin\theta)^2 + (2w\cos\theta)^2\right]^2}. \tag{B5}$$

Accordingly, the RCS deviation and the FGF to elevation angle can be written as, respectively,

$$\delta'^{\mathrm{EC}}_{\mathrm{elev}}(\theta) = \frac{1}{\left[(h/2w)^2\sin^2\theta + \cos^2\theta\right]^2} \tag{B6}$$

and

$$g'_{\mathrm{EC}}(\theta) = \frac{1}{(h/2w)^2\sin^2\theta + \cos^2\theta}. \tag{B7}$$

Using the Taylor series approximation at a small angle and retaining the second-order terms, (B6) and (60) can be reduced to

$$\delta'^{\mathrm{EC}}_{\mathrm{elev}}(\theta) \approx \left\{1 - \left[(h/2w)^2 - 1\right]\theta^2\right\}^2 \tag{B8}$$

and

$$g'_{\mathrm{EC}}(\theta) \approx 1 - \left[(h/2w)^2 - 1\right]\theta^2 \tag{B9}$$

where w should also satisfy the limited range in (A15).

In order to verify the formula, the numerical calculation of the RCS deviation versus elevation angles from 0° to 10° with a step of 0.1° for a 15-in diameter SEC calibrator is shown in Fig. 27, where the solid, dashed-dotted, and dotted lines denote the results calculated using MoM for HH polarization, formulas (54) and (B8), respectively.

It is seen from Fig. 27 that, for the SEC calibrator, the RCS deviation calculated using (54) is extremely close to that calculated using MoM with the error less than 0.01 dB within 10° elevation angle at a higher frequency band, as well as the result calculated by (B8) with the error less than 0.015 dB within 2° elevation angle. The comparison results demonstrate that (54) is precise enough such that it can be used for simulated calculation, while (B8) is simple enough to be used for theoretical analysis, such as the calibration uncertainty in GPR.

C. RCS Comparison of Multiple Calibrators

To further demonstrate the merits of the new EC calibrator, the RCS characteristics are compared with some others that have been traditionally used and recently proposed in the dedicated literature, including SCC, squat spheroidal cylinder (SSC), and metal sphere, listed in Table V. Except for EC-2, all of the calibrators are 15 in in diameter. EC-2 is a compromise design of RCS level, angular sensitivity, CPI, and volume, whose volume is similar to the 15-in sphere.

TABLE V
MULTIPLE CALIBRATORS FOR RCS CHARACTERISTICS COMPARISON

Calibrator	Diameter (inches)	Height (inches)	Width (inches)
SCC	15	7	—
EC-1 (SEC)	15	7	1.5
EC-2	13.38	13.38	1.89
SSC	15	7	3.5
Sphere	15	—	—

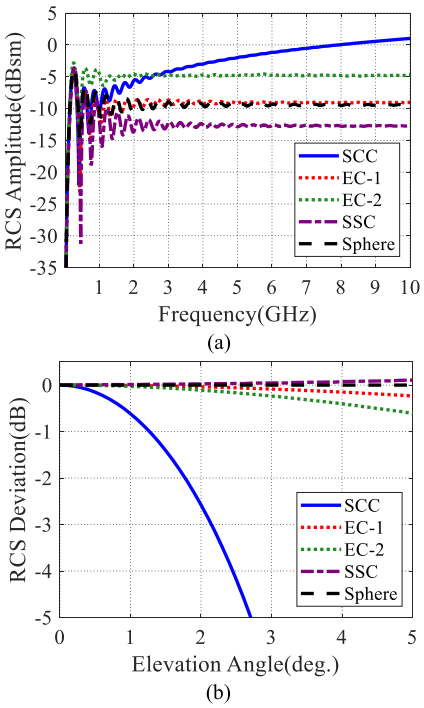

Fig. 28. RCS characteristics of multiple calibrators for HH polarization. (a) RCS amplitude. (b) RCS deviation to the elevation angle at 10 GHz.

The RCS amplitude from 10 MHz to 10 GHz with a 10 MHz frequency step for HH polarization is illustrated in Fig. 28(a), calculated using MoM by FEKO software. The comparison of RCS sensitivity to the elevation angle at 10 GHz frequency for HH polarization of the calibrators is shown in Fig. 28(b).

It can be concluded from Fig. 28(a) and (b) that, by controlling the three geometrical parameters, the proposed EC calibrator can be made to be large enough at the RCS level with a compromised angular sensitivity suitable enough for practical uses, which is significant in exact RCS measurements under a test field with moderate background clutter.

REFERENCES

[1] *IEEE Recommended Practice for Radar Cross-Section Test Procedures*, Standard 1502-2020, Dec. 2020, pp. 1–78.
[2] E. F. Knott, *Radar Cross Section Measurements*. New York, NY, USA: Van Nostrand Reinhold, 1993.

[3] X. Xu, "RCS calibration technique for targets," in *New Techniques for Radar Target Scattering Signature Measurement and Processing*. Beijing, China: National Defense Industry Press, 2017, pp. 119–203.
[4] H. M. Chizever, R. J. Soerens, and B. M. Kent, "On reducing primary calibration errors in radar cross section measurements," in *Proc. Antenna Meas. Tech. Assoc. Symp. (AMTA)*, Sep. 1996, pp. 383–388.
[5] P. Wu and X. Xu, "Improved calibration technique for quasi-monostatic polarimetric measurement system using a dihedral as the calibration reference," *IEEE Trans. Antennas Propag.*, vol. 67, no. 11, pp. 7040–7049, Nov. 2019.
[6] J. A. Stratton, *Electromagnetic Theory*. New York, NY, USA: McGraw-Hill, 1941.
[7] B. M. Kent, K. C. Hill, and W. D. Wood, "Accuracy and calibration sensitivity for AFRL squat cylinder RCS calibration standards," in *Proc. Antenna Meas. Tech. Assoc. Symp. (AMTA)*, Oct. 2000, pp. 387–392.
[8] P. S. P. Wei, A. W. Reed, C. N. Ericksen, and R. K. Schuessler, "Measurements and calibrations of larger squat cylinders," *IEEE Antennas Propag. Mag.*, vol. 51, no. 2, pp. 205–212, Apr. 2009.
[9] X. Xu, Z. Xie, and F. He, "Fast and accurate RCS calculation for squat cylinder calibrators [measurements corner]," *IEEE Antennas Propag. Mag.*, vol. 57, no. 1, pp. 33–41, Feb. 2015.
[10] P. Wu and X. Xu, "Calibration error analysis of squat cylinders for RCS measurement on ground plane range," in *Proc. Int. Conf. Meas., Inf. Control*, May 2012, pp. 282–285.
[11] Y. Z. Liu, X. Xu, and G. Xu, "MIMO radar calibration and imagery for near-field scattering diagnosis," *IEEE Trans. Aerosp. Electron. Syst.*, vol. 54, no. 1, pp. 442–452, Feb. 2018.
[12] B. M. Kent *et al.*, "Design and analysis of a new angularly insensitive RCS calibration device," in *Proc. Antenna Meas. Tech. Assoc. Symp. (AMTA)*, 2002, pp. 202–207.
[13] Z. Li, J. Wu, Z. Wang, S. Wang, and G. He, "A novel calibrator for radar cross section measurement," *IEEE Antennas Wireless Propag. Lett.*, vol. 18, no. 2, pp. 260–263, Feb. 2019.
[14] L. Liang and X. Xu, "A multipurpose calibrator in radar cross section measurement," in *Proc. IEEE Int. Symp. Antennas Propag. USNC/URSI Nat. Radio Sci. Meeting*, Jul. 2018, pp. 2291–2292.
[15] W. D. Wood, P. J. Collins, and T. Conn, "The CAM RCS dual-cal standard," in *Proc. Antenna Meas. Tech. Assoc. Symp. (AMTA)*, 2003, pp. 400–403.
[16] S. Naiva, C. M. Baumgartner, T. Conn, and P. J. Collins, "Implementation of a CAM as a radar cross section (RCS) dual-calibration standard," in *Proc. Antenna Meas. Tech. Assoc. Symp. (AMTA)*, 2007, pp. 82–87.
[17] C. Monzon, "A cross-polarized bistatic calibration device for RCS measurements," *IEEE Trans. Antennas Propag.*, vol. 51, no. 4, pp. 833–839, Apr. 2003.
[18] A. Olk, K. Ben Khadhra, and T. Spielmann, "Highly accurate fully-polarimetric radar cross section facility for mono- and bistatic measurements at W-band frequencies," in *Proc. Antenna Meas. Techn. Assoc. Symp. (AMTA)*, Oct. 2017, pp. 1–6.
[19] M. E. Bechtel, "Short-pulse target characteristics," in *Atmospheric Effects on Radar Target Identification and Imaging*, H. E. G. Jeske, Ed. Dordrecht, The Netherlands: Reidel, 1976, pp. 3–53.
[20] G. T. Ruck, D. E. Barrick, W. D. Stuart, and C. K. Krichbaum, "Ellipsoids and ogives," in *Radar Cross Section Handbook*, vol. 1. New York, NY, USA: Plenum Press, 1970, pp. 341–375.
[21] M. P. do Carmo, "The geometry of the Gauss map," in *Differential Geometry of Curves and Surfaces*, 2nd ed. New York, NY, USA: Dover, 2016, pp. 136–219.
[22] FEKO. (2014). *EM Software & Systems-S.A. Stellenbosch, South Africa*. Accessed: Feb. 27, 2015. [Online]. Available: http://www.feko.info
[23] E. F. Knott, J. F. Shaeffer, and M. T. Tuley, *Radar Cross Section*, 2nd ed. Raleigh, NC, USA: Scitech Publishing, 2004.
[24] A. Michaeli, "Elimination of infinities in equivalent edge currents—Part I: Fringe current components," *IEEE Trans. Antennas Propag.*, vol. AP-34, no. 7, pp. 912–918, Jul. 1986.
[25] J. W. Burns, E. I. Lebaron, and G. G. Fliss, "Characterization of target-pylon interactions in RCS measurements," in *IEEE Antennas Propag. Soc. Int. Symp. Dig.*, Jul. 1997, pp. 144–147.
[26] D. W. Powers, "Characterization of the target-mount interaction in radar cross section measurement calibrations," M.S. thesis, Dept. Elect. Comp. Eng., AFIT, Air Force Base, OH, USA, 2004.
[27] P. Chen, X. Xu, and Y. Jiang, "Comparison of methods to extract target scattering from scattering of target-metal pylon combination," in *Proc. Int. Radar Conf.*, Oct. 2014, pp. 1–6.
[28] K. Naishadham and J. E. Piou, "A robust state space model for the characterization of extended returns in radar target signatures," *IEEE Trans. Antennas Propag.*, vol. 56, no. 6, pp. 1742–1751, Jun. 2008.
[29] K. Naishadham and J. E. Piou, "Analytical characterization and validation of creeping waves on dielectric coated and perfectly conducting cylinders," *Radio Sci.*, vol. 45, no. 5, pp. 1–19, Oct. 2010.
[30] F. He and X. Xu, "A comparative study of two target scattering center models," in *Proc. IEEE 11th Int. Conf. Signal Process.*, Oct. 2012, pp. 1931–1935.
[31] R. E. Kell, "On the derivation of bistatic RCS from monostatic measurements," *Proc. IEEE*, vol. 53, no. 8, pp. 983–988, Aug. 1965.

Tianjin Liu was born in Shandong, China, in 1996. He received the B.S. degree from the School of Information Science and Technology, Dalian Maritime University, Dalian, Liaoning, China, in 2019. He is currently pursuing the Ph.D. degree in signal and information processing with the School of Electronics and Information Engineering, Beihang University, Beijing, China.

His research interests include radar cross section (RCS) measurements, polarimetric calibration, and radar imaging.

Xiaoyu He was born in Jiangxi, China, in 1991. He received the B.S. degree from the School of Mechanical and Electric Engineering, Guangzhou University, Guangzhou, China, in 2012, and the Ph.D. degree in signal and information processing from the School of Electronics and Information Engineering, Beihang University, Beijing, China, in 2018.

He is currently a Lecturer with the School of Electronics and Information Engineering, Beihang University, where he was mainly involved in research of characteristic modeling for multispectral and hyperspectral imagery, radar system modeling, and signal processing.

Xiaojian Xu was born in Jiangxi, China, in 1963. He received the B.S. degree from the Hefei University of Technology, Hefei, China, in 1983, the M.S. degree from the Beijing Institute of Environmental Features (BIEF), Beijing, China, in 1986, and the Ph.D. degree from the University of Nebraska–Lincoln, Lincoln, NE, USA, in 2002, all in electrical engineering.

From 1986 to 1999, he was with BIEF, where he was mainly involved in research of electromagnetic scattering modeling and microwave imaging. From June 1999 to December 2002, he was with the Environmental Remote Sensing Laboratory, University of Nebraska–Lincoln, where his research work was on ultrawideband random noise radar with emphasis on foliage and ground penetration applications. Since January 2003, he has been with the School of Electronic and Information Engineering, Beihang University, Beijing, as a Signal and Information Processing Professor. His research interests include remote-sensing signatures, radar imagery, target recognition, and system modeling.